4.3 Cavity Outlines

The PIV results have highlighted a vortex that forms mid way down the cavity during collapse. To examine the effect the vortex is on the collapse of the cavity, 2D outlines of the cavity from each flow regime were complied. Each example is broken into two sections, the expansion phase and collapse phase with the time from initial impact shown on each outline. The details of the impacts are shown in Table 4.2.

Table 4.2 Impact details of the image sequences used for the cavity outlines

Impact Number	Image Sequence	Regime	Fr	We	Re	t_c
CO-I	33g-01-80	Primary vortex ring regime	111	66	2849	1.40
CO-II	33g-01-160	Pre-entrapment jetting	174	100	3463	1.10
CO-III	33g-01-220	Primary bubble entrapment	219	121	3778	0.97
CO-IV	33g-01-340	Primary bubble entrapment	325	180	4600	0.80
CO-V	33g-01-460	Post-entrapment jetting	423	242	5386	0.71
CO-VI	33g-01-760	Post-entrapment jetting	654	372	6669	0.57

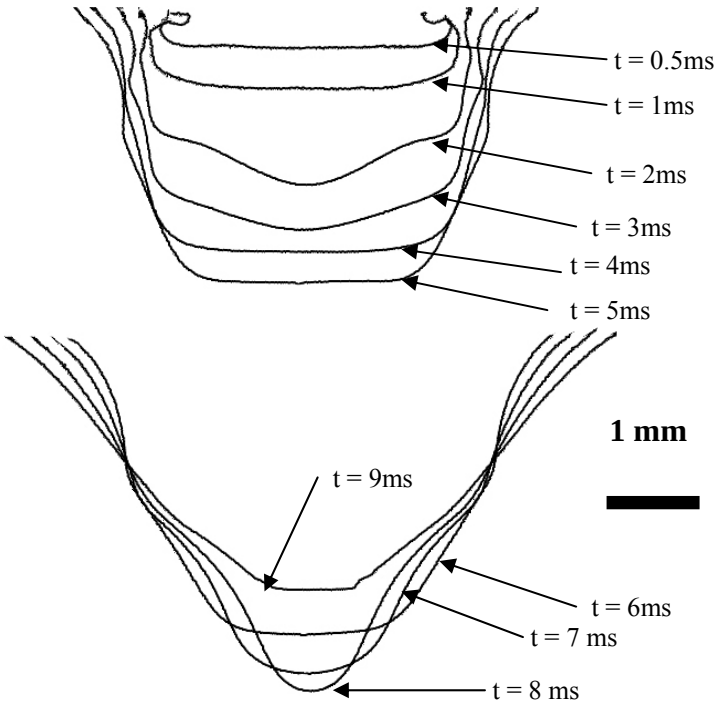

Figure 4.9 Cavity outlines for CO-I Primary vortex ring regime (Fr = 111, We = 66, Re = 2849, t_c = 1.40)

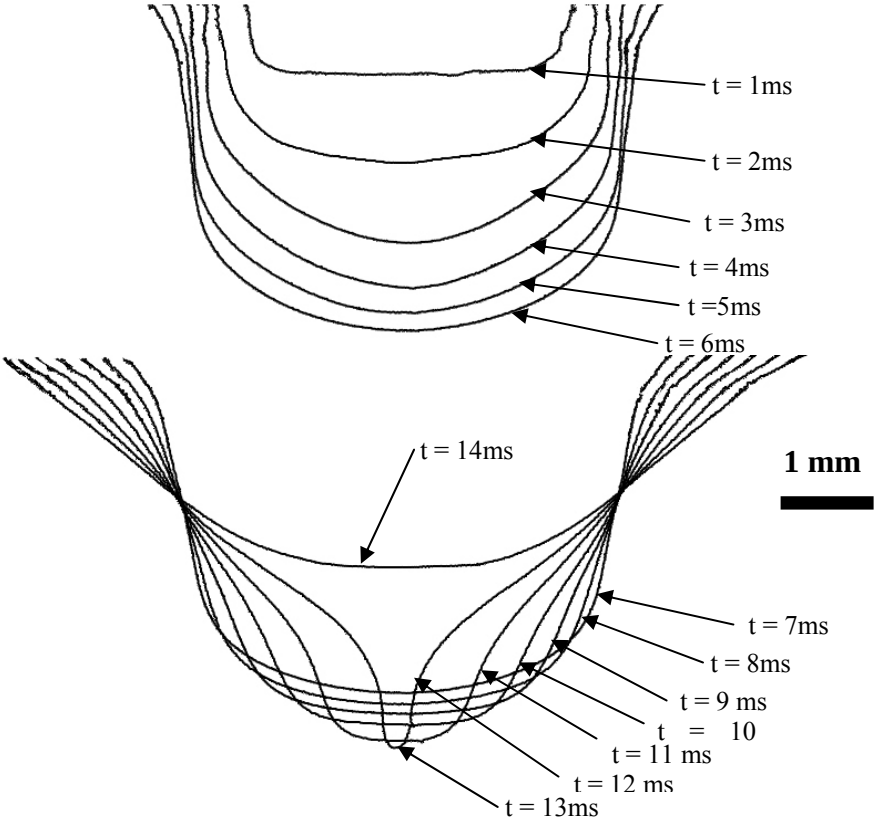

Figure 4.10 Cavity outlines for CO-II Pre-Entrapment Jetting (Fr = 174, We = 100, Re = 3463, t_c = 1.10)

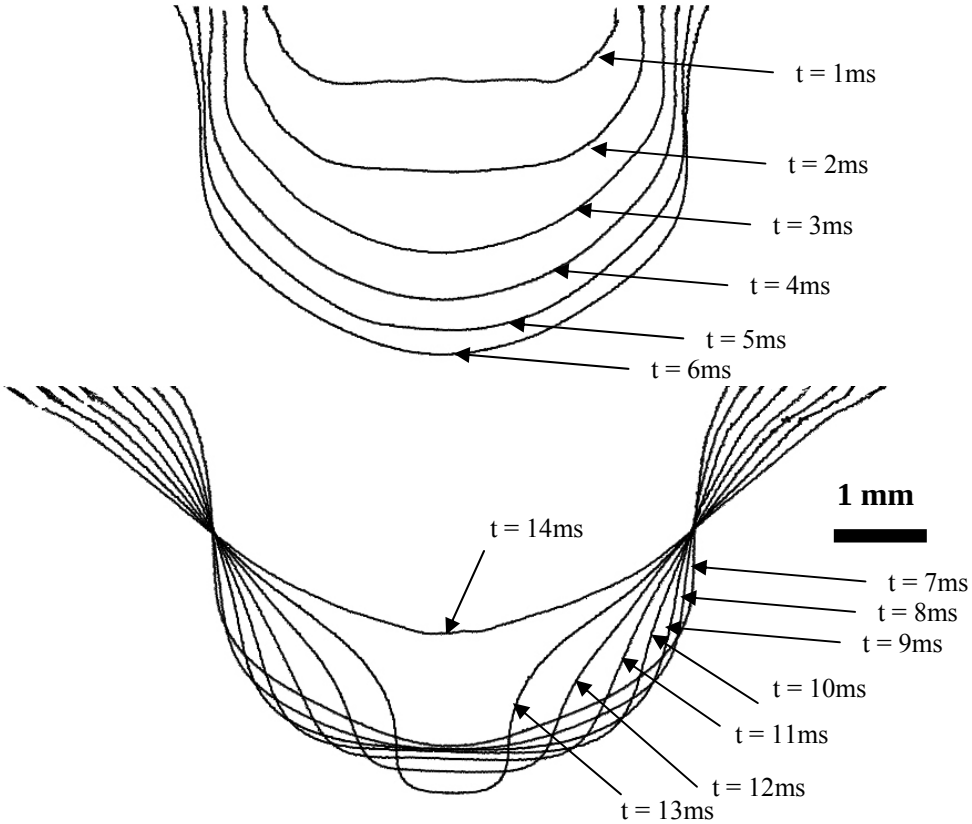

Figure 4.11 Cavity outlines for CO-III Primary Bubble Entrapment (Fr = 219, We = 121, Re = 3778, t_c = 0.97)

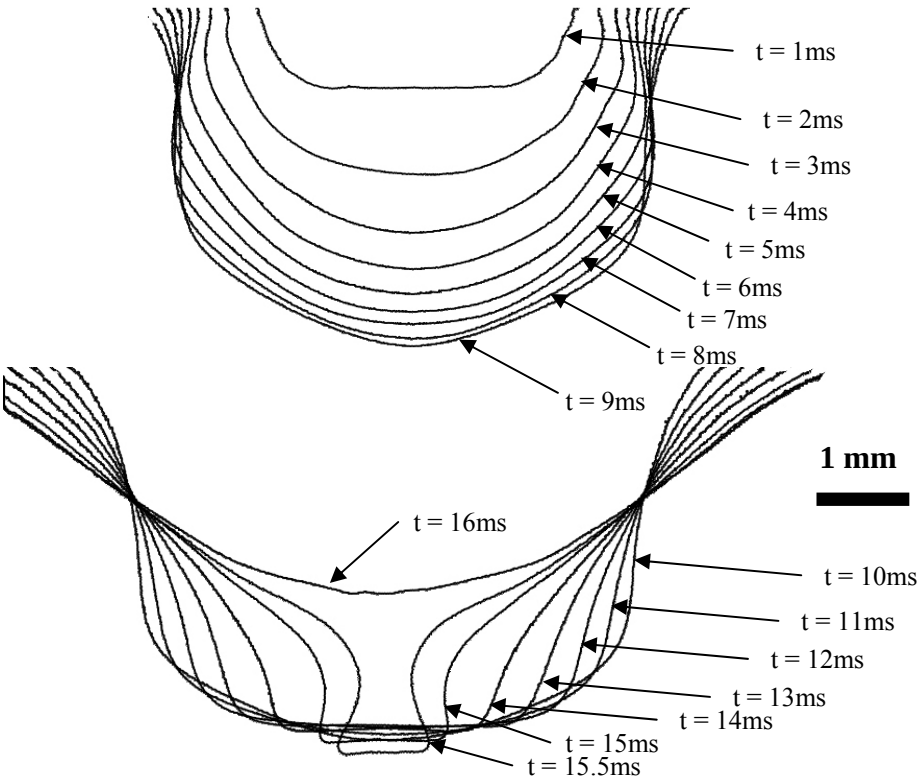

Figure 4.12 Cavity outlines for CO-IV Primary Bubble Entrapment (Fr = 325, We = 180, Re = 4600, t_c = 0.80)

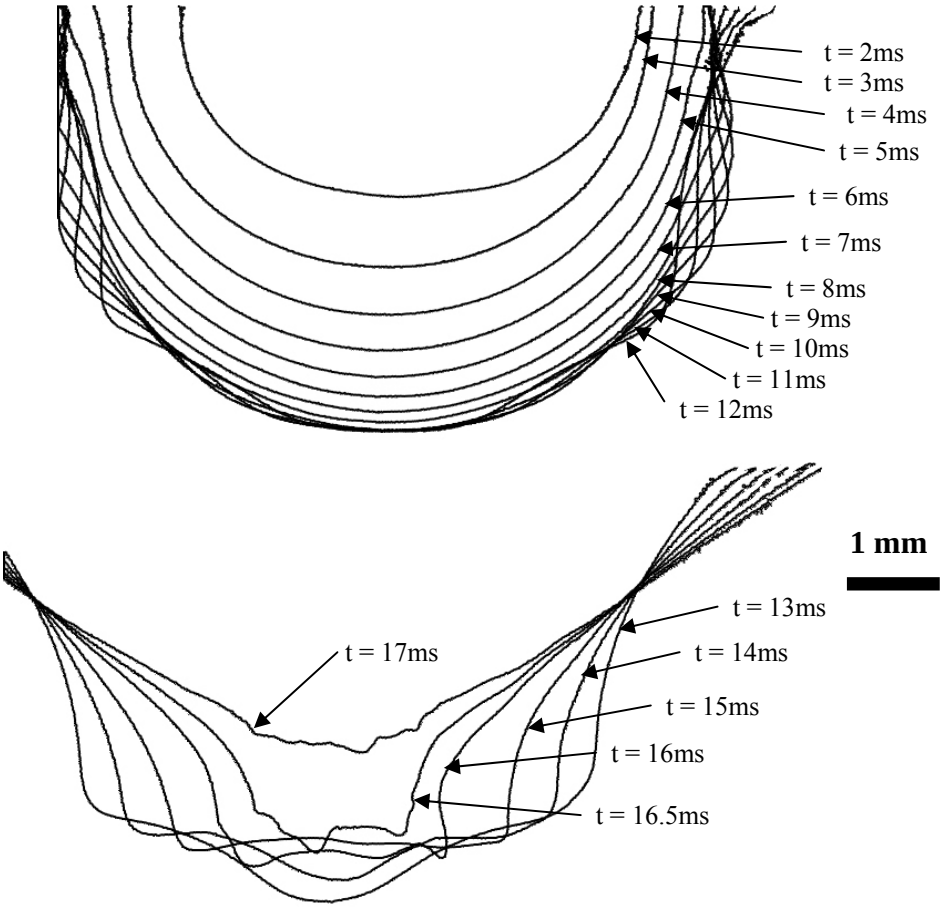

Figure 4.13 Cavity outlines for CO-V Post-Entrapment Jetting (Fr = 423, We = 242, Re = 5386, t_c = 0.71)

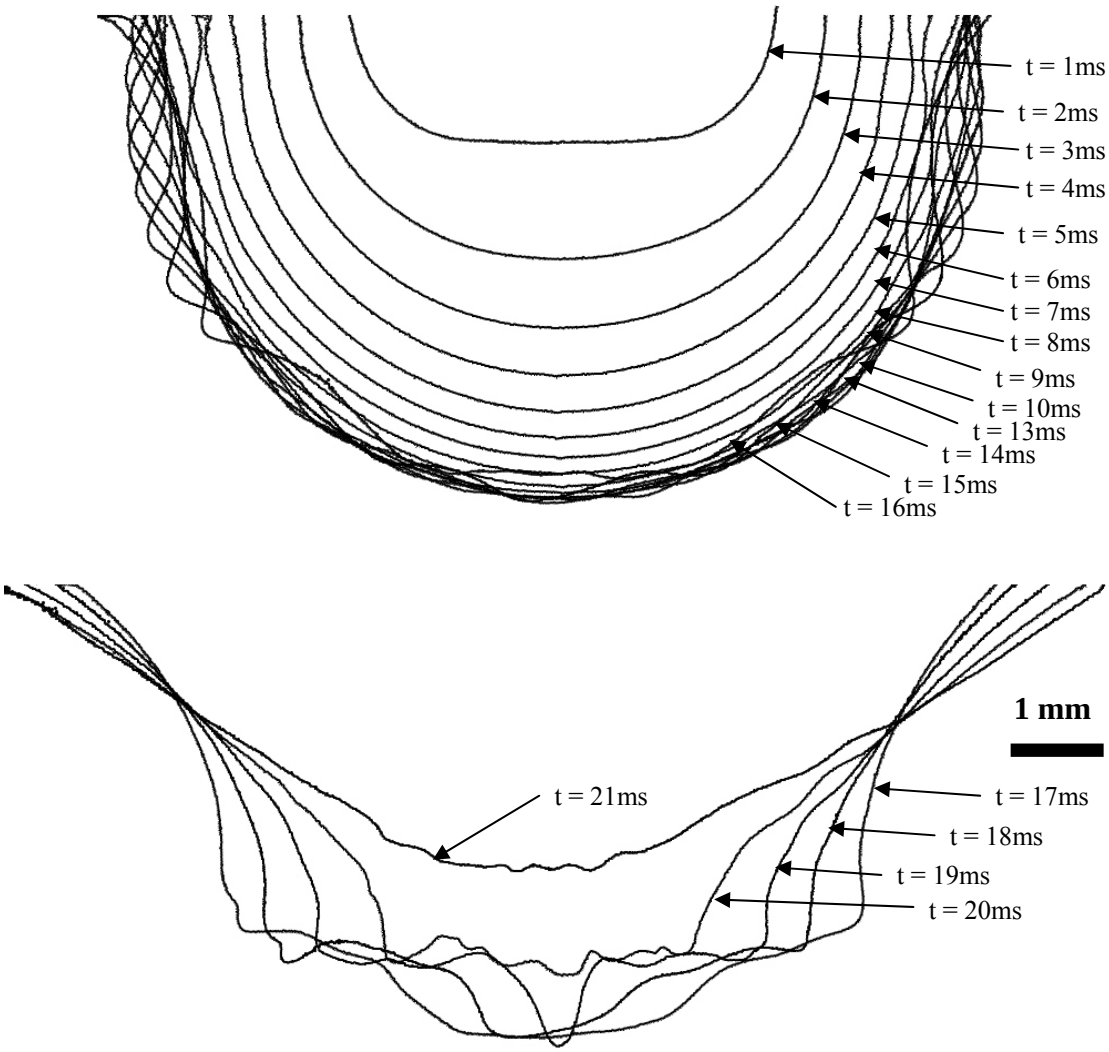

Figure 4.14 Cavity outlines for CO-VI Post-Entrapment Jetting (Fr = 654, We = 372, Re = 6669, t_c = 0.57)

Examining the above cavity outlines the obvious feature that attracts attention is the two stationary points on either side of the cavity that form during the collapse phase. From the PIV results there appeared to be a location around which the cavity would rotate during collapse but it was not clear if this location moved over time or remained stationary. The stationary points are similar to a zero point occupied by a standing wave. From the cavity outlines, the stationary point forms after the cavity walls have ceased growing and the cavity begins to collapse. Therefore, the distance between the two stationary points should give an accurate measure of the maximum cavity width. It is important to note that since the cavity is axisymmetric the two stationary points visible in these 2D images actually form part of a larger stationary line that encompasses the whole cavity. Some properties of the stationary line will be further examined in section 4.4.

The other important observation from the above images is the tendency of the cavity to form in a cylindrical cavity or dome shape cavity at low impact velocities (Figure 4.9 - Figure 4.12). Classical descriptions of the cavity expansion describe it as an axisymmetric hemi-spherical expansion. However, it is clear from the cavity outline images that this is not the case for most of the impacts. Only in the higher velocity impacts (Figure 4.13 and Figure 4.14) does the expansion approaches a hemi spherical shape. Looking at the outlines from Figure 4.11 in closer detail, the rates of expansion in the horizontal and vertical directions appear to be different. That is, over the same time period the base of the cavity grows further than the side walls of the cavity. For example examining the cavity growth between 3ms and 4ms from Figure 4.11, the base grows almost twice the distance of the side walls during the same time period. This observation raises questions about the momentum of the drop is transferred into the bulk fluid for medium to low impact velocities. Assuming a hemi-spherical expansion in these impacts is not indicative of the physics present.

Another interesting observation is the appearance of 3D capillary waves that distort the cavity. The final two images sequences (Figure 4.13 and Figure 4.14) from the post-entrapment regime vividly show how large 3D capillary waves distort the cavities interface. In Figure 4.13 the wave first appears approximately 6ms after initial impact. The cavity continues to expand while the wave converges towards the base of the cavity. At approximately 11-12 ms after initial impact the depth of the cavity begins to stagnate. It should be noted that the capillary waves do not cause the collapse of the cavity but they do change the position of the stationary points.

4.4 Stationary Line

One of the distinguishing features of the cavity outlines was the formation of clear stationary line about which the entire cavity rotates about during the collapse phase. This line is important as its appearance governs when the expanding cavity has reached its maximum width and the collapse phase begins. Thus, the distance between the two stationary points on the cavity outlines should provide an excellent measure of the cavities maximum width. To investigate the properties of the stationary line, the horizontal position and depth of this line was tracked over three different needle types and across a multitude of impact velocities. Figure 4.15 shows the variation of the dimensionless cavity width versus impact Froude number.

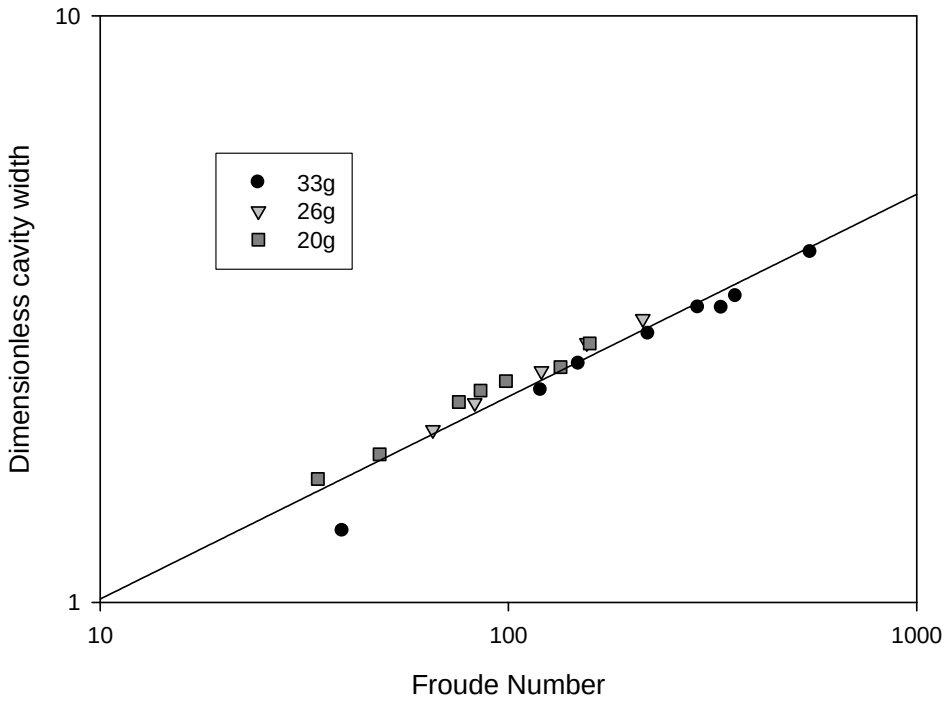

Figure 4.15 Variation of dimensionless width of stationary line versus impact Froude number

In Figure 4.15 the dimensionless maximum cavity width (W_c^*) is defined by the distance between the two stationary points divided by the drop diameter and plotted against impacting Froude number. A least squares fit of the data gives a result of $W_c^* = 0.458Fr^{0.345}$ with a R^2 value of 0.94. Therefore, the maximum cavity width approximately scales as $W_c^{*'} \propto Fr^{1/3}$. Therefore, using a an energy balance between the

kinetic energy of the impacting drop (equation 4.1) and the potential energy for a hemi-spherical the scaling should be the same.

$$W_c^* = D_c^* = 2\left(\frac{Fr}{3}\right)^{1/4} \tag{4.1}$$

However, the expected scaling of $W_c^* \propto Fr^{1/4}$ is clearly at odds with the experimental data gathered in this study of $W_c^* \propto Fr^{1/3}$. The dimensionless maximum depth scaling (D_c^*), cavity depth divided by drop diameter, is now checked to see if it matches expected theory (Figure 4.16).

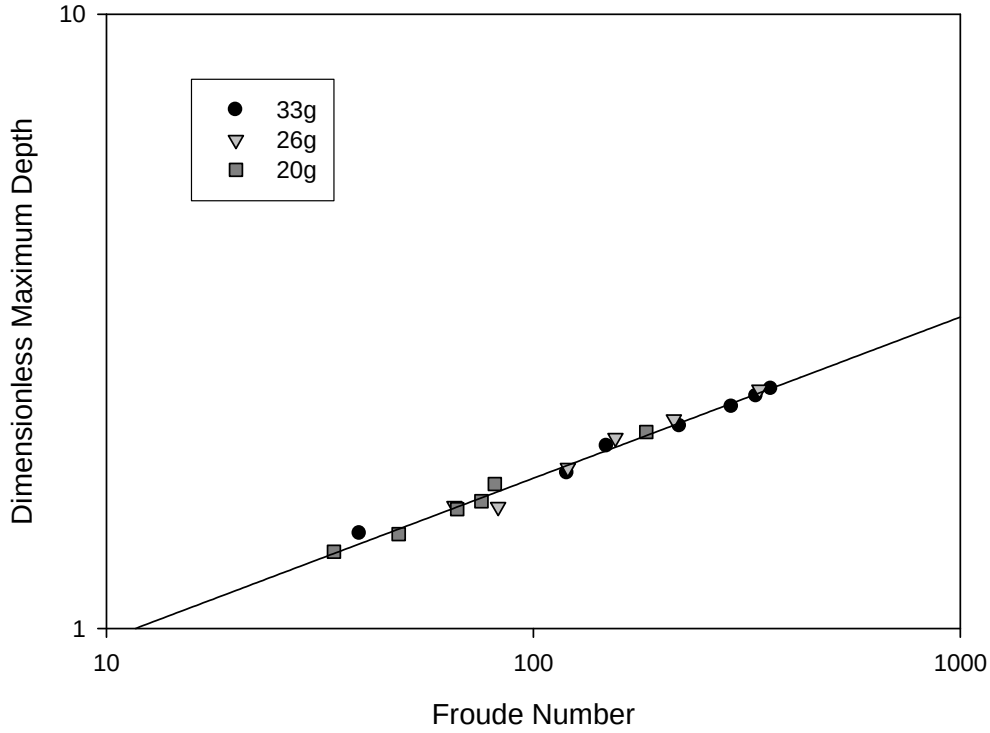

Figure 4.16 Variation of dimensionless maximum cavity depth versus impact Fr number

The least squares line of best for this data in Figure 4.16 gives a result of $D_c^{*'} = 0.524Fr^{0.262}$ with an R^2 value of 0.98. This result matches the expected scaling of $D_c^{*'} \propto Fr^{1/4}$. Therefore, the depth scaling is following expected theory but the width scaling is not. The obvious first question to ask is that there were errors associated with measuring distance between the stationary points may be distorting the scaling. Thus all

data points were recalculated and a slightly higher scaling of $W_c^* \propto Fr^{0.36}$ was found, which is a trivial difference. A new criteria was used to calculate the maximum cavity width assuming that the distance between the two stationary points was not the maximum cavity width. This new criterion involved measuring the point at which the angle between the cavity and free surface rotated away from being perpendicular. Using these values an even worse scaling of $W_c^* \propto Fr^{0.460}$ was obtained. Again this criteria for the maximum cavity width does not follow theory. Another possibility for the discrepancy between theory and experimental results is that the wrong physical assumptions have been made in the energy model. To see if this was the case the width and depth scaling was recalculated for a cylindrical expansion. Where AR is the aspect ration defined as cavity radius (R) divided by cavity depth (H).

$$W_c* = 2\sqrt{AR}\left(\frac{Fr}{6}\right)^{1/4}$$
$$D_c* = \frac{1}{\sqrt{AR}}\left(\frac{Fr}{6}\right)^{1/4} \quad \textbf{(4.2)}$$

From the above equations the scaling of both the maximum depth and width still scale as $Fr^{1/4}$. However, there is no value of AR that give a scaling of $D_c^* \propto Fr^{1/4}$ and $W_c^* \propto Fr^{1/3}$. Even if an additional energy sink (*i.e.* the wave swell) is added to the energy balance the fundamental scaling of the width still remains the same. Therefore, at this stage no theoretical basis for the scaling of the cavity width can be provided. This is a rather troubling conclusion because understanding why this stationary line scales the way it does is vital in understanding many of the other phenomena associated with the cavity collapse. It is possible that energy models are no longer sufficient to describe the complex phenomena occurring during collapse and other tools such as non-linear capillary standing wave analysis maybe necessary.

Another peculiar property of the stationary line is the depth at which it forms below the free surface. Examining Figure 4.17 the depth of the stationary line remains essentially constant for each different drop size. Towards the higher Froude numbers for each drop size there is a slight decrease in the height (*i.e.* the stationary point moves upward towards the free surface) and this generally occurs during the transition into the post-

entrapment jetting regime. This behaviour is quite strange in so far as it suggests that the depth at which the cavity rotates about is solely dependant on drop size and not impact velocity. This suggests that wavelength of the initial disturbance on the free surface (*i.e.* impacting drop diameter) is a governing factor in how the cavity collapses, since drop diameter will be proportional to the wavelength of any surface waves created. This is by no means a conclusive explanation for the phenomena observed and a more thorough investigation is required.

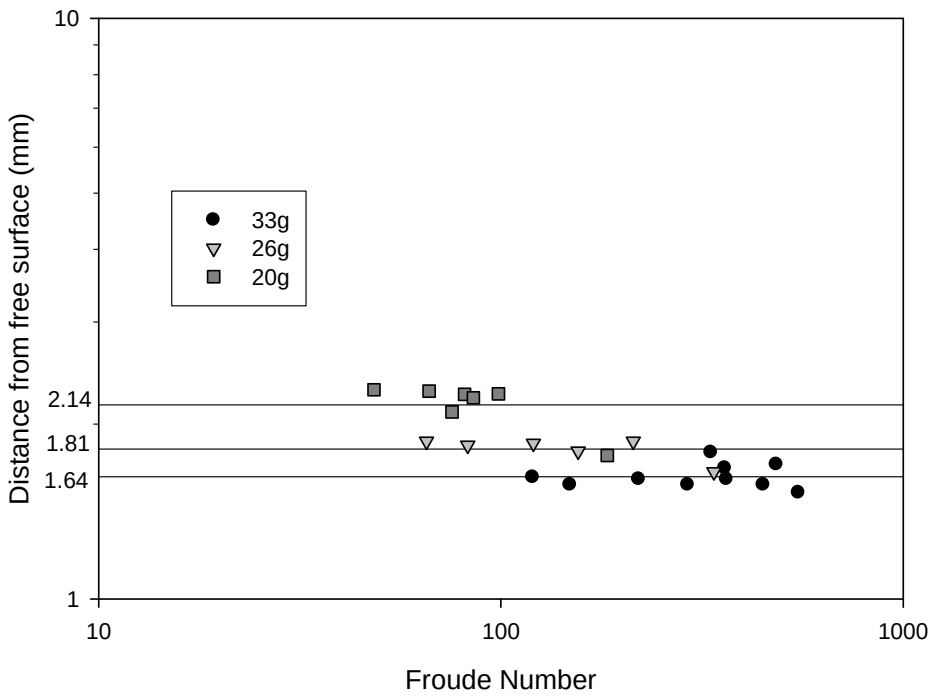

Figure 4.17 Variation of stationary line depth with impact velocity. Solid lines are the mean distances

4.5 Cavity Formation and Collapse Flow Model

Examining all the above PIV and cavity outline evidence a general flow model for the cavity expansion and collapse can be put forward. This six stage model includes

- Expansion and wave swell growth
- Peak wave swell height
- Wave swell drainage
- Cavity base stagnation
- Vortex formation
- Flow convergence along centreline

The results from PIV Impact III is used to demonstrate the different stages of cavity formation and collapse. All other impacts PIV impacts show similar characteristics and can be observed in their respective image sequences in section 4.2.

4.5.1 Expansion and wave swell growth

The flow field around the expanding cavity 3 ms after initial impact is shown in Figure 4.18. The first property of the flow field to explore is the direction of the velocity vectors around the cavity. Near the free surface the flow is directed upward and feeds the wave swell that is forming above the free surface. The reason for this behaviour is that a lower density fluid (air) resides above the pool and has less inertial resistance than the bulk fluid (water). Thus, the inertia of the impact will drive the bulk fluid upward along the path of least resistance and rather than trying to compress the fluid nearby. The fluid must also be displaced upward for the conservation of mass to be satisfied. Accompanying the upward flow are two vortices that form on each side of the cavity (Figure 4.19) and rotate in opposite directions to each other. The upward flow extends to about 2-3mm below the free surface. Past this point the velocity vectors are initially parallel to the free surface before pointing downward at greater depths. These vectors will curve back toward the free surface in the far field as a by product of the bulk fluid conserving mass. However, the far field is not visible in these images.

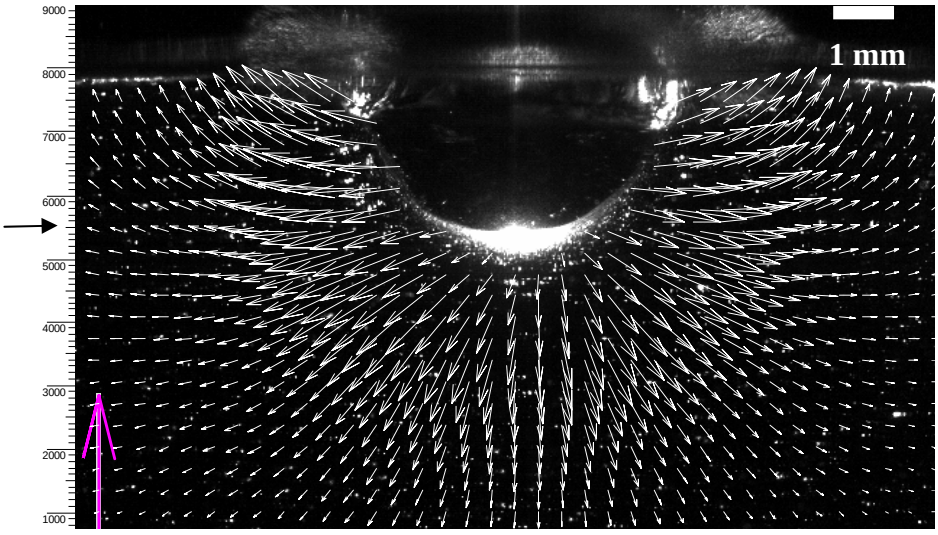

Figure 4.18 Flow field during cavity expansion (Reference vector 0.25 m/s)

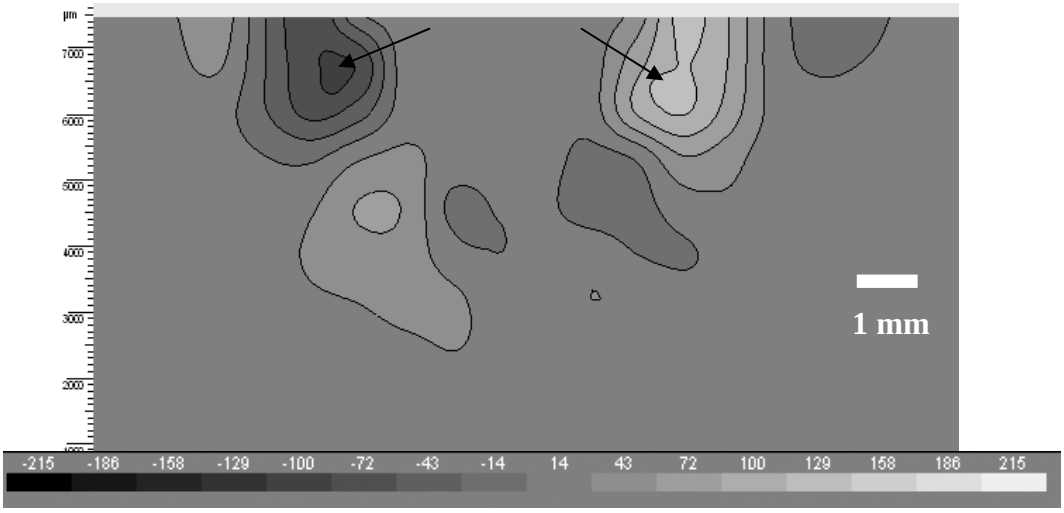

Figure 4.19 Vorticity map during cavity expansion (sec^{-1})

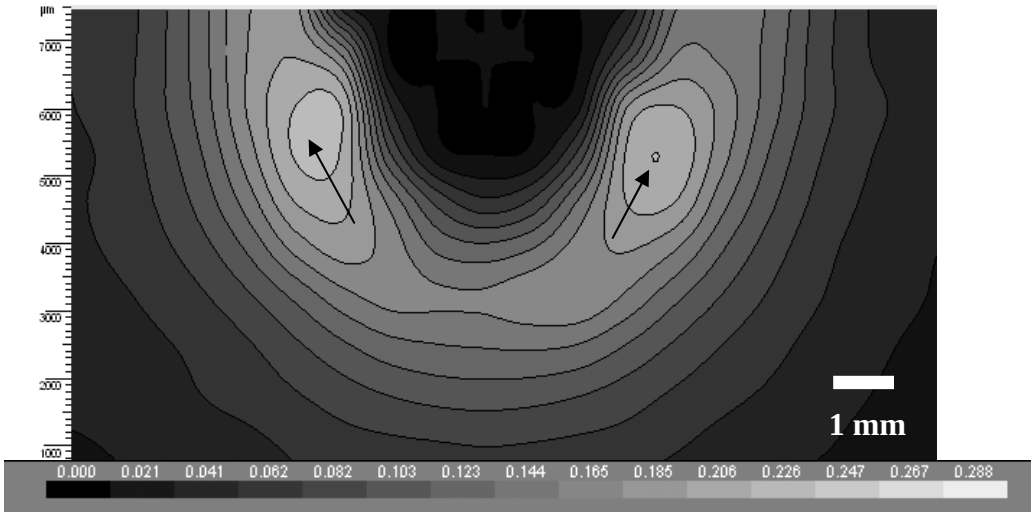

Figure 4.20 Velocity magnitude during cavity expansion (m/s)

In terms of the velocity magnitude around the cavity there is no uniform radial expansion as one would expect in a hemi-spherical expansion (Figure 4.20). Rather close of the cavity near the mid point of the cavity there are two high relatively high velocity concentrations. This would tend to indicate that the transfer of the drops energy into the bulk fluid is not uniform around the cavity. Rather, the energy transfer appears to be concentrated at the bottom of the cavity. This non-uniform distribution of energy was also noted by Elmore *et al.* (2001). There is also a steep velocity gradient between these high velocity areas and the cavity interface. This is due to the FlowManager software interpolating between the masked area of the cavity, which has no velocity, and the high velocities areas so that there is no discontinuity in the shading levels, thus making the sharp velocity gradient an aberration. Moving out radially from the two high zones of velocity the flow field becomes more uniform with almost a hemi-spherical shape for each band.

Previously it was observed that the near the top of the cavity the velocity vectors were directed toward the free surface. Below this line the vectors were orientated towards the bottom of the pool. In this area, away from the cavity interface, surface tension and gravitational will dominate. Therefore, extracting the length scale from the Bond number should give us some insight into the depth at the which the free surface effects will subside.

$$h = \sqrt{\frac{\sigma}{\rho g}} = \sqrt{\frac{0.073}{(998)(9.81)}} = 2.73mm \qquad \textbf{(4.3)}$$

Thus, if only surface tension and gravitational forces are acting on the particles a short distance away from the cavity one would expect the transition between vectors pointing upward and the vectors pointing downward to form around 2.73 mm below the free surface. To verify if this, a number of measurements of the horizontal line of vectors were taken over several impacts. The horizontal line fluctuated over the images in each PIV image sequence. Therefore, the maximum and minimum depth of the horizontal line was recorded for each impact and averaged (Table 4.3).

Table 4.3 Depth of free surface influence

Needle Size	Height	Min depth of free surface influence (mm)	Max depth of free surface influence (mm)	Average depth of free surface influence (mm)
33g	20	2.40	3.10	2.75
33g	60	2.30	3.00	2.65
33g	100	2.00	3.70	2.85
33g	140	1.80	2.80	2.30
33g	160	2.30	2.70	2.50
33g	200	2.30	3.00	2.65
33g	320	2.65	3.40	3.03
33g	360	2.80	3.30	3.05
33g	500	2.70	3.00	2.85
33g	620	2.50	2.80	2.65
			Average	2.73

The results from Table 4.3 show the average depth of the horizontal velocity vectors to be centred around the length scale predicted by the Bond number (Equation 4.3). This upward flow field a distance away from the cavity can be explained by the presence of capillary driven surface waves. Thus during the expansion phase of cavity development the region around the cavity can be broken into three different regions as schematically shown in Figure 4.21. Close to the cavity's interface the flow is primary driven by the inertia supplied by the initial impact. A short distance away from the cavity the flow becomes surface tension driven, near the surface, and gravity driven deep within the fluid. The most important point to note here is that the free surface will heavily influence how the cavity and wave swell will develop. Therefore, one would expect changes in surface tension to have profound effects on the expansion and subsequent collapse.

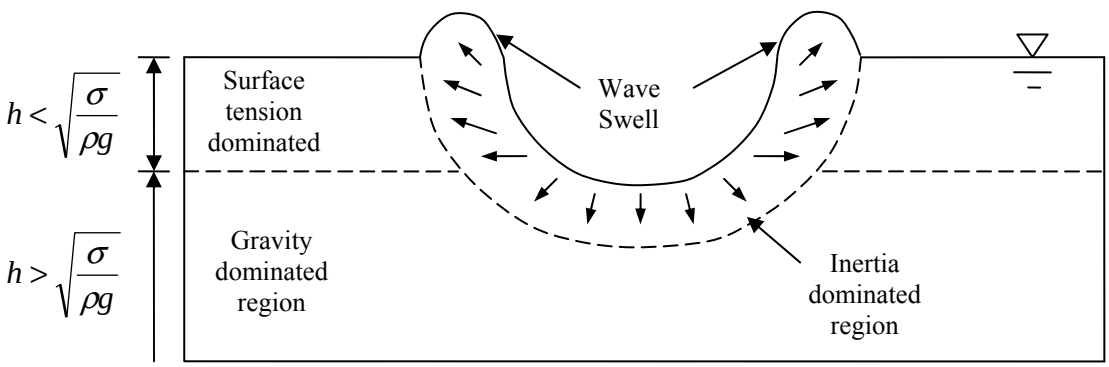

Figure 4.21 Flow regions during cavity expansion

4.5.2 Peak wave swell height

The next stage of the cavity collapse occurs when the wave swell reaches its maximum height. This is best visualised in Figure 4.22 where the velocity vectors near the free surface are parallel with the free surface. This indicates that the energy source that was driving fluid into the wave swell has ceased. That is, the portion of the kinetic energy from the impact that was directed outward in the horizontal, has been fully converted into potential energy in the wave swell. While the fluid flowing into the wave swell has ceased, the cavity walls do not stop expanding. The momentum of the fluid in the wave swell continues to pull the cavity outward while the cavity continues to expand downward (Figure 4.22). A schematic representation of the cavity during this stage is shown in **Error! Reference source not found.**.

In Figure 4.24 two relatively high zones of velocity magnitude persist near the base of the cavity like in Figure 4.20. This further adds weight to the argument that the momentum distribution is not uniform during expansion. Logically, if the momentum distribution were relatively uniform one would expected that all points of the cavity would stagnate at a similar point in time. However, from the PIV results here show that this is clearly not the case. Just how this non-uniform behaviour occurs is not clear at this stage. However, an important consideration maybe understanding how the final portion of the drop coalesces with the bulk fluid. Recall from Chapter 3, the down cavity images that showed the top portion of the drop was visible for a significant period of time after initial impact (Figure 3.28 (Page 119)). The implication of this is that as the cavity expands, the final portion of the drop will provide a small but continuously depleting energy source that will assist with the downward expansion. Furthermore, as the cavity grows downward and the final portion of the drop moves downward thus it becomes less and less likely that any of the fluid within this portion of the drop will be driven upward or sideways to provide any side wall expansion. Thus, leading to the non-uniform expansion of the cavity. Further understanding of this phenomena will require numerical simulations and the superposition of velocity data upon the drops fluid distribution in and around the cavity. Experimental techniques such as PIV or LIF (Laser Induced Fluorescence) will not be suitable as they cannot visualise what is occurring inside the cavity during collapse.

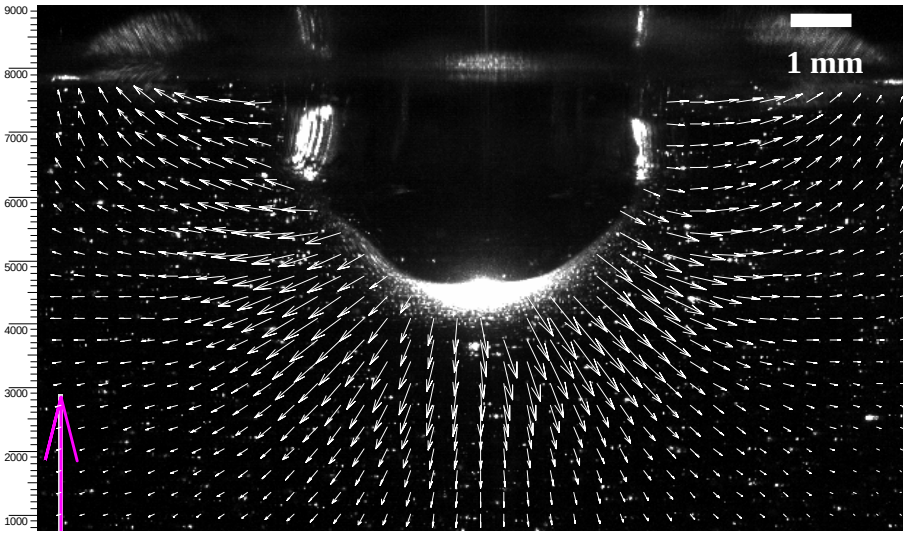

Figure 4.22 Flow field during wave swell stagnation (Reference vector 0.25 m/s)

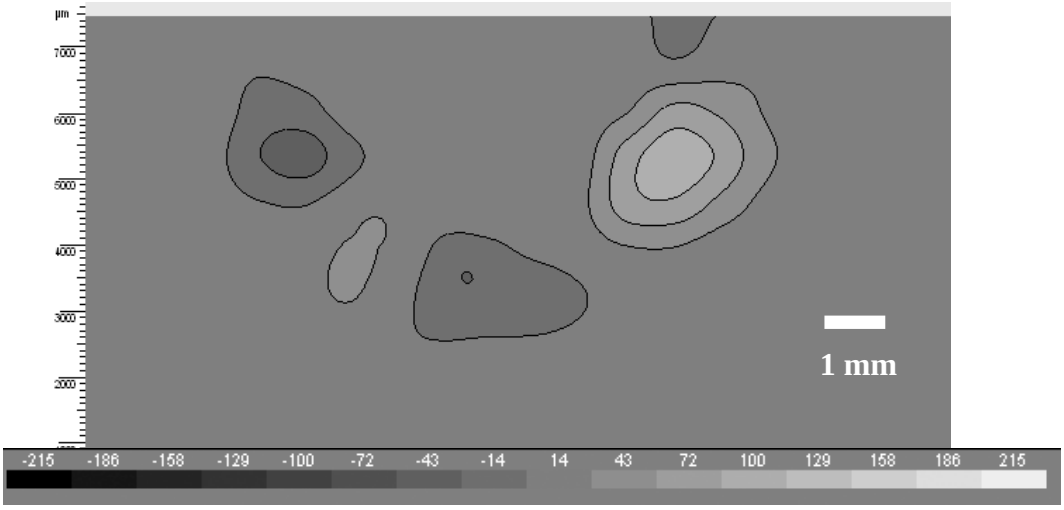

Figure 4.23 Vorticity map during wave swell stagnation (sec^{-1})

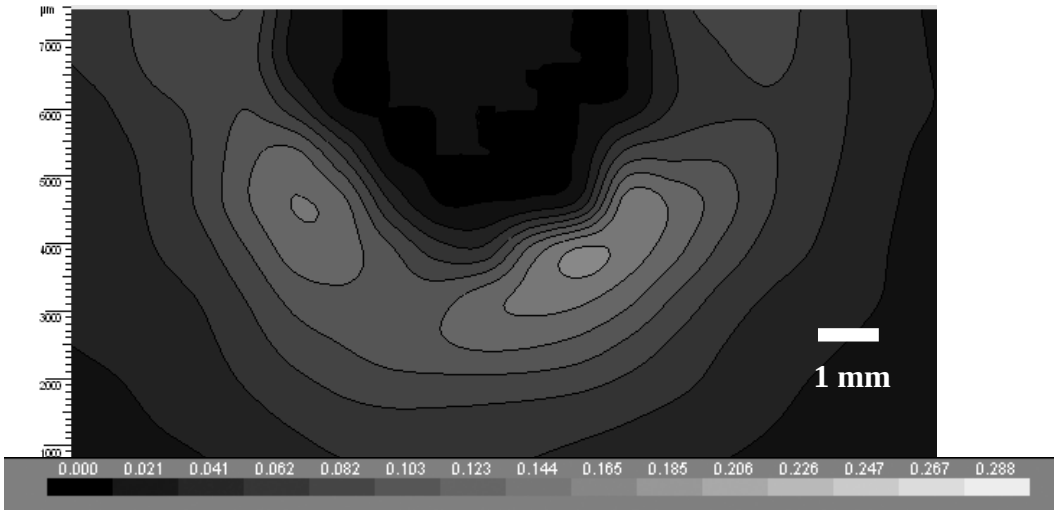

Figure 4.24 Velocity magnitude during wave swell stagnation (m/s)

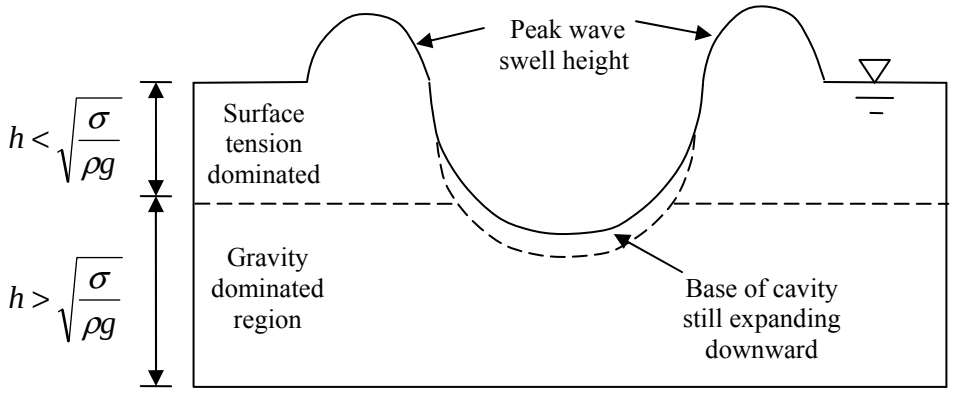

Figure 4.25 Flow regions at peak wave swell height

4.5.3 Wave swell drainage

Since the growth of the wave swell has ceased, gravity now acts on the fluid in the wave swell to drain the wave swell. This effect can be observed in Figure 4.26 where the vectors near the top of the cavity, which were previously parallel to the free surface, are now pointing downwards and away from the cavity. Again the outward motion of the fluid is due to the momentum of the wave swell. The downward component of the velocity is due to gravity which will be described shortly. Also during this time the base of the cavity is still expanding so the fluid near the base of the cavity is also being displaced downward (Figure 4.28). During this stage of cavity development and collapse there is little vorticity present (Figure 4.27).

The time scale from the Froude number can give some insight into the relative importance of the intertial and gravitational time scales with respect to each other. (Equation 4.4). The characteristic length scale used to determine the expected time scale is the cavity half width. This is defined as the horizontal distance from the stationary line to the cavity centreline. The collapse time is defined as the time from when the stationary line first forms to the point where the cavity base begins to retract. Based on these definitions a comparison between the experimentally measured collapse times and the collapse times defined by the Froude number time scale have been compiled in Table 4.4. The experimental data is taken from the 2D cavity outlines shown in section 4.3.

$$t = \sqrt{\frac{L}{g}} \tag{4.4}$$

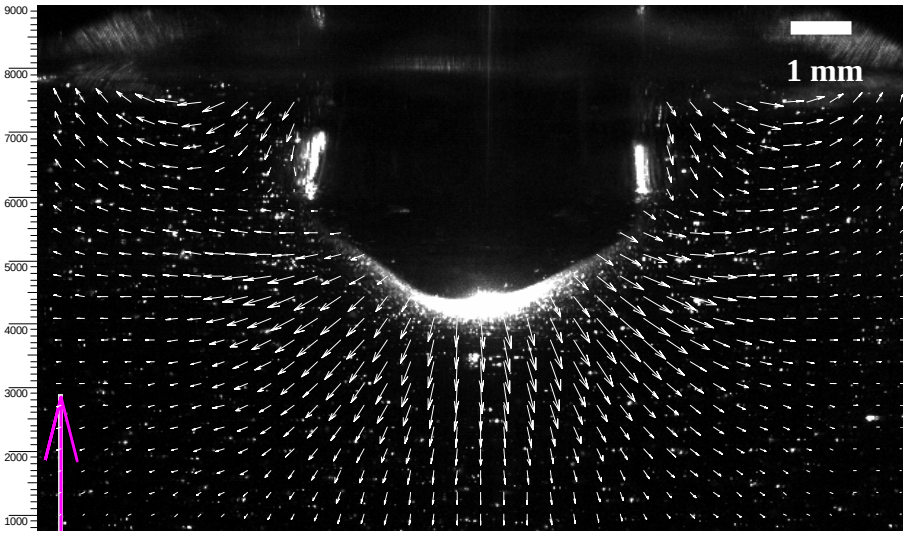

Figure 4.26 Flow field during wave swell drainage (Reference vector 0.25 m/s)

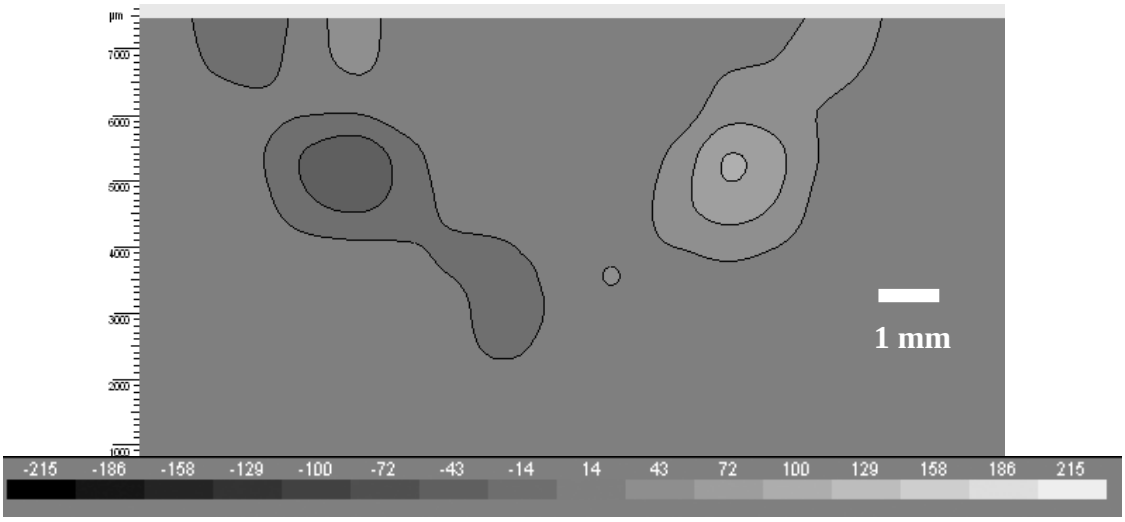

Figure 4.27 Vorticity map during wave swell drainage (sec^{-1})

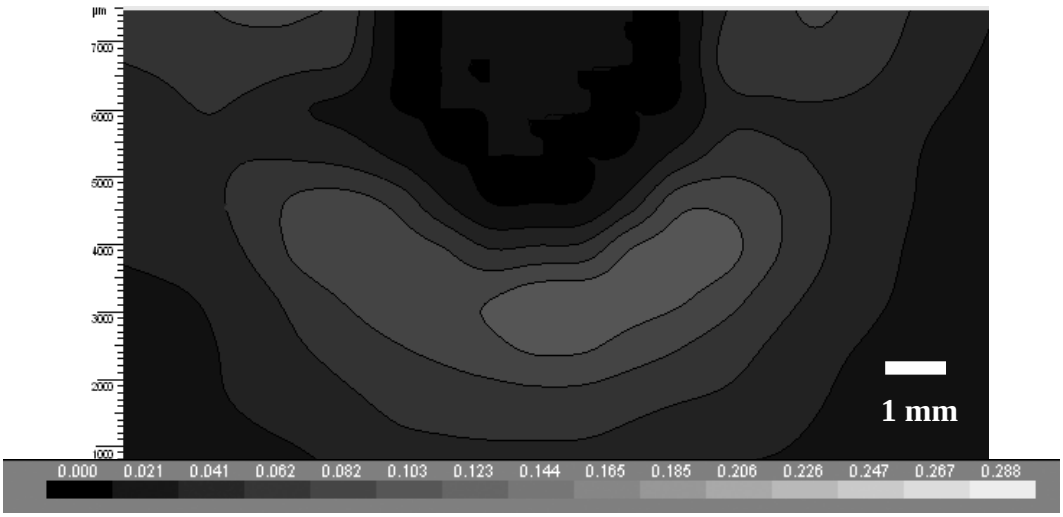

Figure 4.28 Velocity magnitude during wave swell drainage (m/s)

Table 4.4 Comparison between experimental cavity collapse times and predicted values

Impact Sequence	Regime	Cavity Half Width (mm)	Expansion Time (ms)	Collapse Time (ms)	Total Time (ms)	Time scale from Fr Number
33g-01-80	Primary Vortex	1.88	5	4	9	13.8
33g-01-160	Pre-Entrapment	2.33	6	7	13	15.4
33g-01-220	Primary Bubble	2.64	6	8	14	16.4
33g-01-340	Primary Bubble	3.04	9	7	16	17.6
33g-01-460	Post-Entrapment	3.29	12	5	17	18.3
33g-01-760	Post-Entrapment	3.90	16	5	21	19.9

Examining Table 4.4 several trends are apparent. The collapse time is in the same order of magnitude as the time scale from the Froude number indicating that the collapse is a balance of gravitional and intertial forces. However, the collapse time is slightly variable over range of impacts examined here. These discrepancies more than likely arise from errors in defining when the collapse actually starts and ends. We have already seen from the PIV results that as the wave swell begins to drain the cavity is still expanding downward. Thus one could argue that this point in time should be taken as the start of cavity collapse as gravity governs the drainage. In the post-entrapment examples the collapse time is slightly lower than the collapse time in the pre-entrapment and primary bubble entrapment regimes. This is due to capillary waves distorting the cavities interface where the stationary line forms and thus delaying the formation of a distinct stationary line. This error would be in the order of 2-3 ms, which would make that the collapse time roughly constant for the higher regimes (pre-entrapment, bubble entrapment and post-entrapment). A schematic representation of the flow field during this stage of cavity development is shown in Figure 4.29.

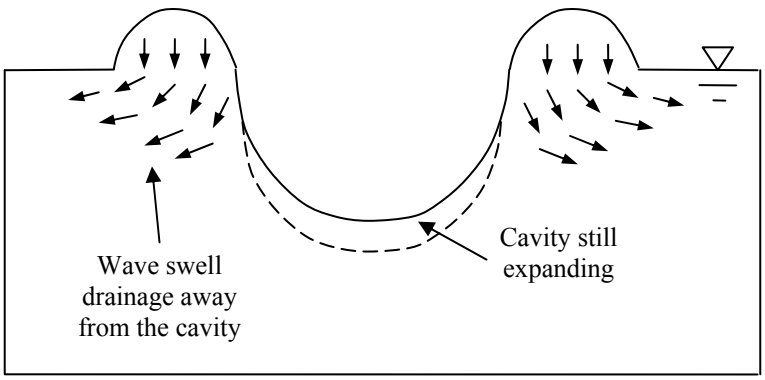

Figure 4.29 Direction of the flow draining from the wave swell

4.5.4 Cavity base stagnation

When the energy from the initial impact has been dissipated cavity growth ceases. This can be seen in Figure 4.32 where the magnitude of the velocity is approaching zero at the base. Meanwhile the velocity magnitude near the top of the cavity is increasing in velocity due to the previously described effect of gravity. The fluid in this region also changes direction (Figure 4.30). The air inside the cavity provides little inertial resistance to the heavier fluid travelling down from the wave swell. Thus the cavity begins to collapse. It is interesting to note that the first part of the cavity to move inwards are the "lower corners" of the cavity and not the cavity base, as indicated by arrows. How these "lower corners" move inward relative to the cavity base is a critical element in explaining why bubble entrapment occurs along with the different types of jetting and will be discussed in section 4.5.6. The vorticity development at this stage of the collapse process is also minimal (Figure 4.31). The flow field is schematically shown in Figure 4.33.

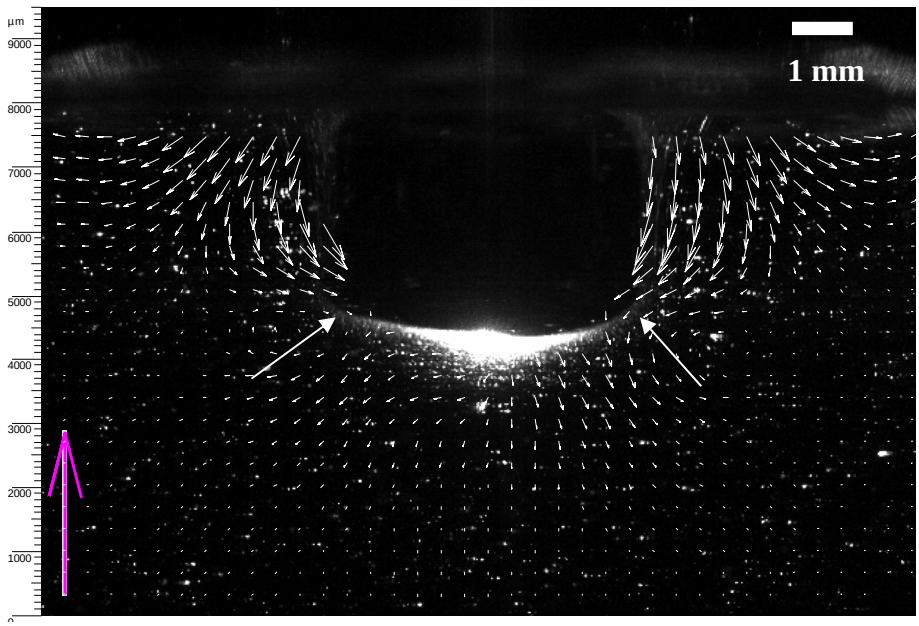

Figure 4.30 Flow field during cavity base stagnation and collapse initiation (Reference vector 0.25 m/s)

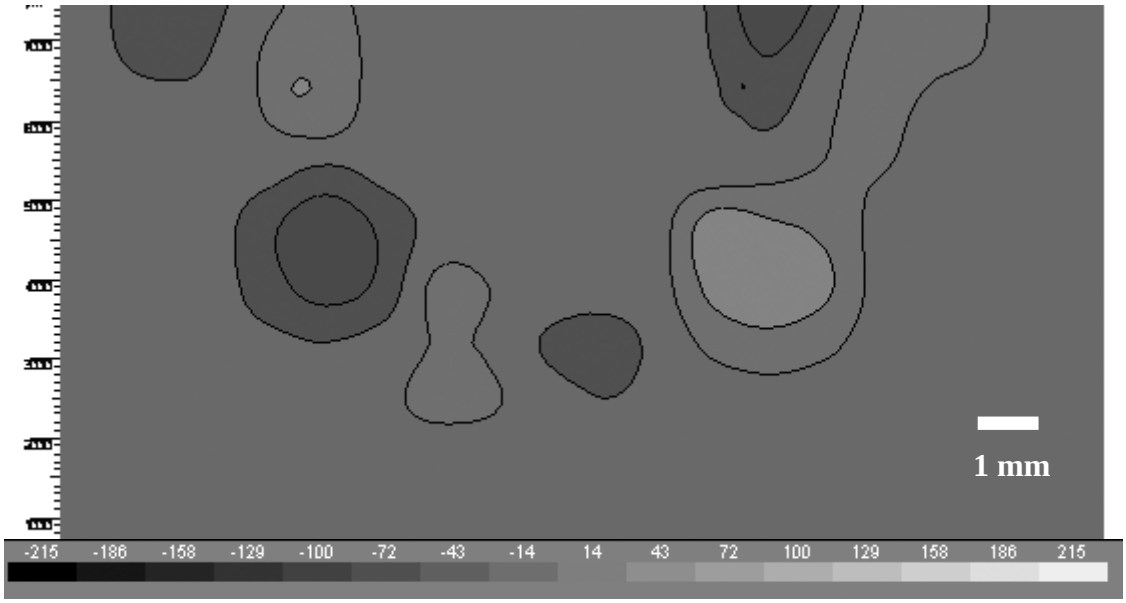

Figure 4.31 Vorticity map during cavity base stagnation and collapse start (sec^{-1})

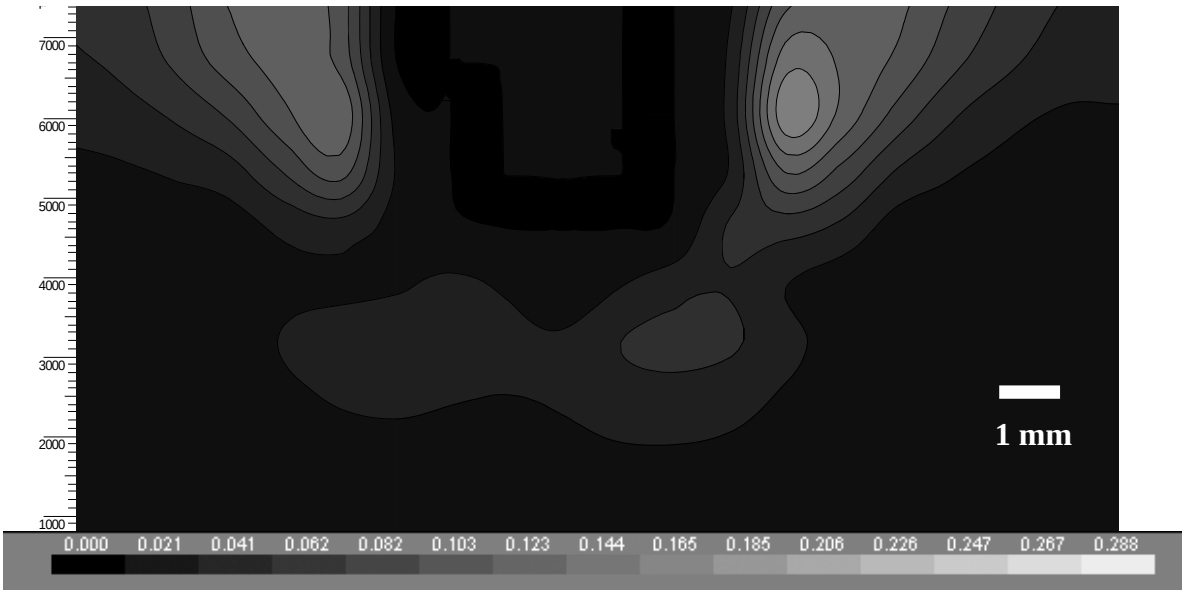

Figure 4.32 Velocity magnitude during base stagnation and collapse initiation (m/s)

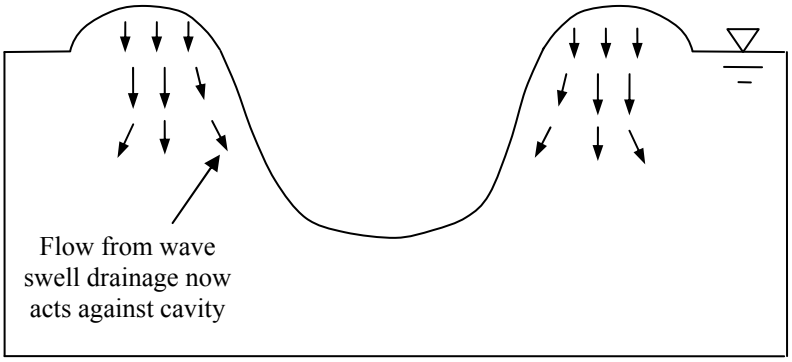

Figure 4.33 Flow direction around cavity as the base of the cavity stagnates

4.5.5 Vortex formation

As the base of the cavity is squeezed inward by the flow originating from the wave swell, a strong rotational flow field forms (Figure 4.30). This leads to the formation of a vortex which is centred approximately 1.5-1.6 mm below the surface (Figure 4.31). This is the same depth as the stationary line was shown to form in Figure 4.17. Thus, it can be postulated that the vortex is responsible for forming the stationary line observed in the 2D cavity outlines. The velocity magnitude during this stage of the collapse is also relatively high (Figure 4.32). A schematic illustration of how the flow field around the cavity is shown in Figure 4.37.

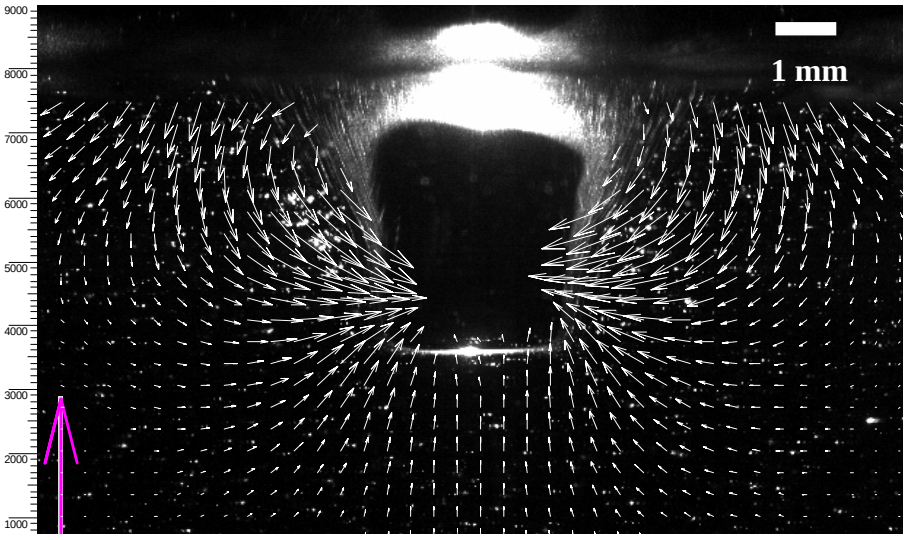

Figure 4.34 Flow field during flow reversal and collapse (Reference vector 0.25 m/s)

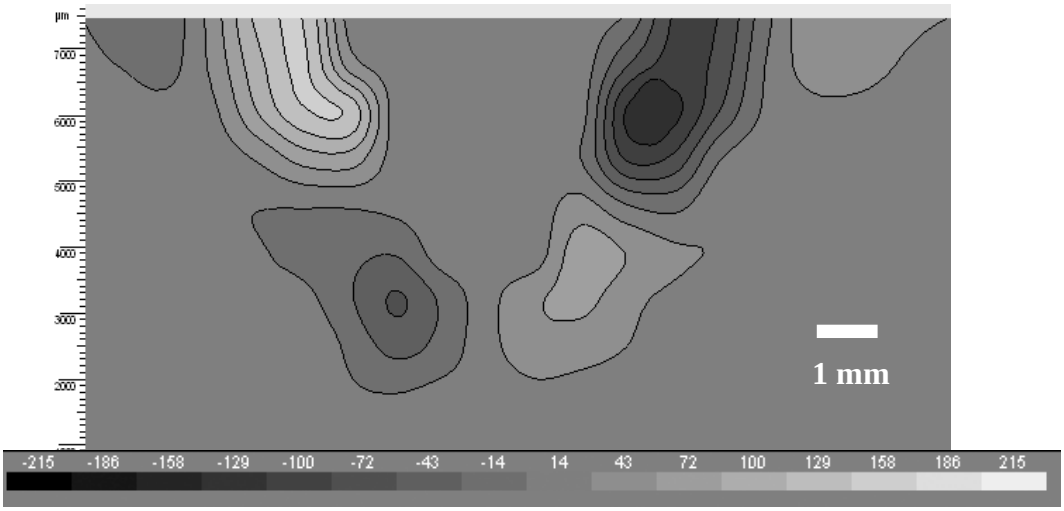

Figure 4.35 Vorticity map during flow reversal and collapse (sec^{-1})

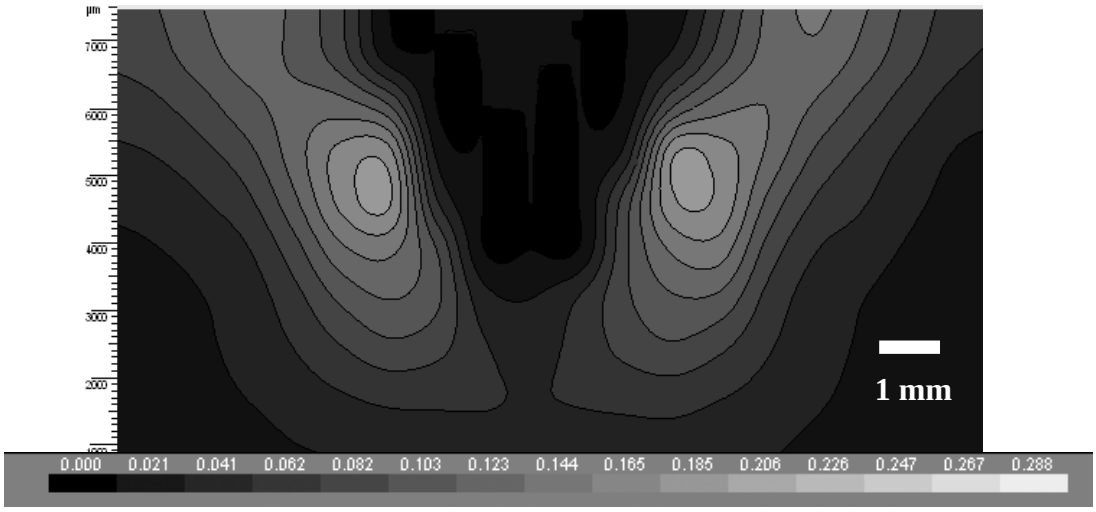

Figure 4.36 Contours of velocity magnitude during flow reversal and collapse (m/s)

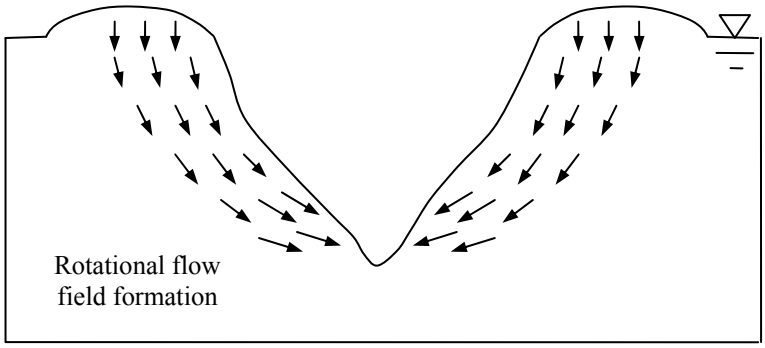

Figure 4.37 Vortex formation around the collapsing cavity

4.5.6 Flow convergence along centreline

The final stage in the cavity's life is the convergence of the fluid being driven by the vortex along the centre line of the cavity. How the flow converges at the base of the cavity is vital in understanding much of the secondary phenomena associated with the cavity collapse (*i.e.* jetting and bubble entrapment). All of the previous steps in the cavity collapse process have been described in the generic sense. That is, each stage has similar characteristics regardless of regime. However, how the flow converges along the centreline of the cavity profoundly changes in each different flow regime. What appears to be the key element in understanding what type of jetting or bubble entrapment occurs, is the direction of the flow around the cavity as it meets along the centreline. This is best demonstrated by a comparison of the flow fields in different regimes as the fluid converges along the centreline.

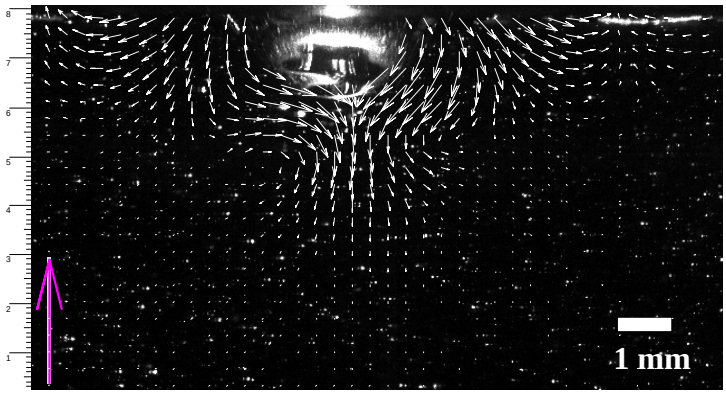

Figure 4.38 Flow field during downward convergence

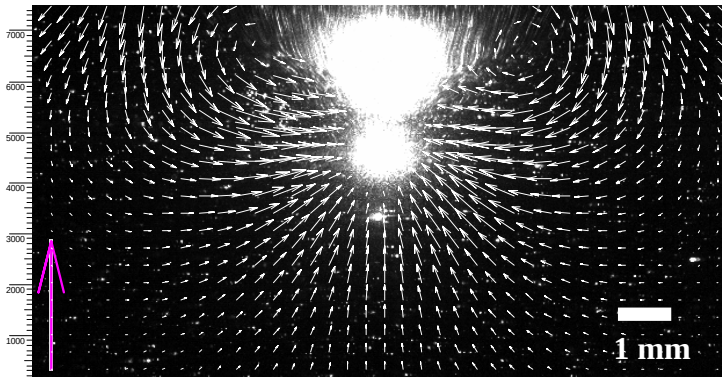

Figure 4.39 Flow field during parallel flow convergence

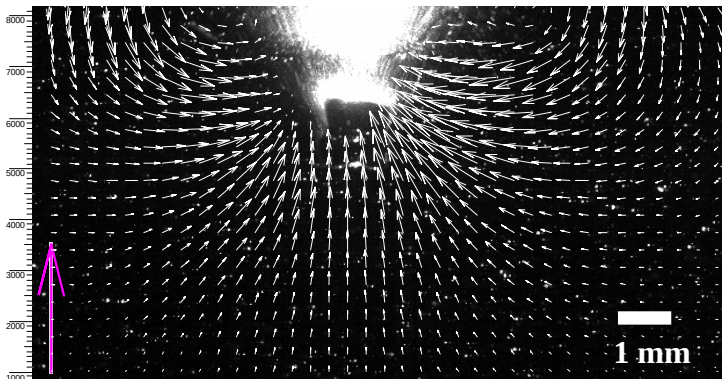

Figure 4.40 Flow field during upward convergence

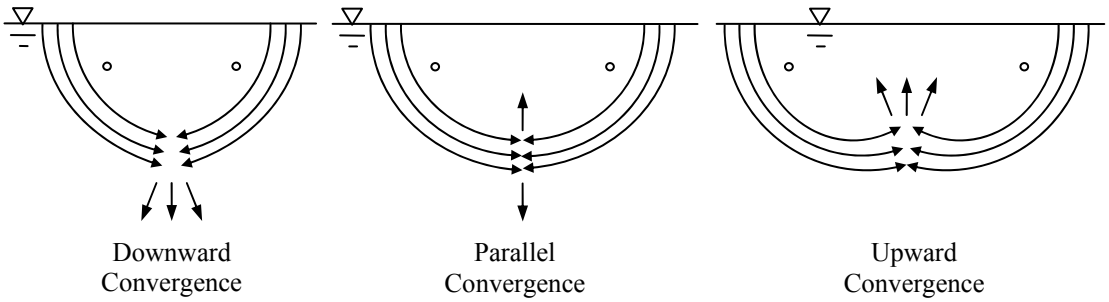

Figure 4.41 Flow convergence conditions

In the primary vortex ring regime the fluid near the base of the cavity has a strong downward component as it converges (Figure 4.38). This is due to the cavity not being very wide. Thus the vortex that is controlling the collapse does not rotate the fluid significantly before it converges along the centreline of the cavity. In the pre-entrapment jetting regime and primary bubble entrapment regime the flow meets almost parallel to the horizontal (Figure 4.39). Here the cavity width is slightly wider than the cavity in the primary vortex ring regime. This seems to allow the fluid being driven by the vortex to undergo a larger angular rotation before meeting in the centreline. Thus leading to a parallel convergence condition. Finally, in the post entrapment jetting regime the flow meets with a strong upward velocity component (Figure 4.40). At these extremely wide cavity widths, the fluid appears to rotate past the horizontal before converging. This leads to the upward convergence flow condition. Thus, it appears the width of the cavity will dictate the direction at which the flow converges at the base. A wider cavity allows the flow to rotate further towards the free surface before converging. Exactly why a larger cavity width allows the fluid to undergo a larger angular rotation before converging requires further investigation. A graphical representation of the different flow convergence conditions is shown in Figure 4.41.

In the next chapter, these three different flow convergence conditions will be used to explain why different types of jetting occur. Therefore, only a brief summary on the effects of the flow convergence will be given here. In the primary vortex ring regime the majority of the fluid will be convected downward after it converges. Therefore, there is little driving force to form jets of any significance. The other consequence of the downward convergence condition is that it may assist in vortex ring formation. In the pre-entrapment jetting and primary bubble formation regime a parallel flow convergence condition occurs. This type of convergence is similar to two parallel jets converging. When two parallel jets converge a stagnation point forms. This in turn will form a high pressure point that will rapidly drive the fluid in orthogonal directions to the original flow direction. Thus giving rise to high speed upward and downward jets. In the post-entrapment jetting regime the flow drives the cavity upward faster than the cavity comes inward. This allows the fluid to converge with a strong upward velocity component along the centreline. This does not give rise to a high pressure point. Therefore, only slow moving thick jets are formed.

4.6 Summary

This chapter has shown the first continuous high speed PIV imaging of the cavity formation and collapse over several different regimes. The impacts across all regimes exhibit similar characteristics that have allowed for the formulation of a general flow model. The first critical element in the development and subsequent collapse of the cavity is how the wave swell above the free surface is formed. The wave swell becomes a critical component of the cavity collapse process as it provides the fluid that creates the velocity gradients responsible for the vortex formation.. Thus, how much fluid is contained in the wave swell and how it is distributed will determine how the collapse occurs. The behaviour of the vortex is the second critical component in cavity collapse process as it essentially dictates how the fluid converges along the axis of symmetry. The vortex was shown to influence the cavity collapse by forming a stationary line about which the cavity rotates during collapse. Some of the properties of the stationary line were examined but no theoretical explanation for its behaviour could be put forward. Finally, the converging fluid was shown to occur with three different flow conditions depending on cavity width. This was postulated to be responsible for the different types of jetting and bubble entrapment seen across various regimes. Thus, in the next chapter a closer examination of the forces that induce jetting in the different regimes will now be explored. The arguments relating to how the flow converges at the base of the cavity will be used to argue why the different modes of jetting occur.